Ultrafast Exciton Motion in Photosynthetic Antenna Systems: The FMO-Complex

Th. Renger and V. May*

Institut für Physik, Humboldt-Universität zu Berlin, Hausvogteiplatz 5-7, D-10117 Berlin, Federal Republic of Germany

Excitation energy transfer in the Fenna−Matthews−Olson (FMO) photosynthetic antenna complex of chlorobium tepidum is investigated theoretically. On the basis of a dissipative multiexciton theory, the numerical simulations reproduce the cw-absorption and, in using the same parameters, the differential absorption of ultrafast pump−probe experiments. Exciton relaxation processes are included via a coupling to the vibrations of the protein matrix. In order take into account a delocalized protein−pigment interaction a correlation radius of the protein vibrations is introduced. The model allows for the study of the temperature dependence of optical spectra and enables one to utilize exciton relaxation data as a probe for a global-shape estimation of the spectral density of low-frequency protein vibrations. In fitting the cw-absorption measured at 5 and 107 K, the strength of the exciton-vibrational coupling, the related correlation radius and spectral density, and the inhomogeneous broadening of the exciton levels are determined anew. The obtained parameters are used to reproduce 150 fs pump−probe spectra as well as transient anisotropy pumped and probed at different wavelengths and different temperatures.

I. Introduction

In recent years, ultrafast spectroscopic techniques have been widely used to study the photosynthetic apparatus of bacteria as well as that of higher plants. In combining the spectroscopic analysis with structural data it is possible to reach a deeper understanding of the functionality in the sub-picosecond time region of these natural molecular nanostructures.

Most success could be achieved in following the different steps of charge separation proceeding in the reaction center of purple bacteria. After the pioneering work of Michel, Huber, and Deisenhofer in clarifying the molecular structure of the bacterial reaction center,[1] a huge amount of data has been accumulated. In the last years structural data have been also offered for the peripheral antenna complexes of the photosystem II of higher plants (LHC-II)[2] and on the antenna complex II of purple bacteria (LH-II)[3], both with a resolution of several angstroms. The highly symmetric structure of the LH-II complex is a topic of femtosecond spectroscopy and, in particular, stimulated a lot of experiments on ultrafast exciton motion, exciton localization, and exciton relaxation (see, e.g. ref 4).

But there already exist structural data of a green bacteria antenna complex for more than 20 years. This complex is known as the Fenna−Matthews−Olson (FMO) complex.[5−7] It is arranged by protein trimers where every protein monomer contains seven bacteriochlorophyll (BChl) molecules. The BChls are more or less uniformly distributed in the protein matrix at a nearest BChl-BChl distance of about 11 Å. In contrast to the broad and structureless Q_y−absorption of the LH−II, the absorption of the FMO-complex shows substructures reflecting delocalized electronic singlet excitations of the various BChls. As in other antenna complexes, these excitations can be described within a Frenkel-exciton model since any charge transfer among different chromophores is absent. This standard exciton concept has been applied by Pearlstein and Lu,[8,9] and recently by Gülen[10] and Louwe et al.[11] to study the linear optical

response measured in ordinary absorption and also in circular and linear dichroism experiments. The protein environment has been taken into account 2-fold. First the BChl transition energies (so-called site energies) are assumed to be shifted due to a different binding site in the protein, and second there is an inhomogeneous distribution of BChl energies at the same site in different FMO monomers. Here we want to present an extension of the standard approach and take into account also the homogeneous spectrum, (i.e., dynamical fluctuations of the BChl site energies).

The distinguishable structures in the cw-absorption and their alternation with temperature favors the FMO-complex to study details of excitation energy (exciton) relaxation. In particular, one can expect to obtain data on some details of the protein vibrations. Since the coupling to these vibrations is not too strong relaxation mainly proceeds via transitions among the exciton levels accompanied by the emission or absorption of *single* vibrational quanta of the protein (the medium the BChls are embedded in). In this manner one can probe the spectral density of the protein vibrations (density of states combined with the distribution of the exciton−vibrational coupling constants).

Related pump−probe experiments in the femtosecond-time region have been carried out recently by Freiberg and co-workers[12] and in the groups of Aartsma[13] and Struve.[14] By exciting an upper level in the manifold of (single-)exciton states, one can detect by a second probe beam tuned to a lower lying exciton state how relaxation appears among the different levels. It is typical for the studied sub-picosecond time region that coherences among different exciton levels have to be considered. Appropriate simulations can be carried out within the dissipative multiexciton model.[15,16]

The measurements in refs 12 and 14 are based on the FMO-complex of Chlorobium tepidum which differs from that of Prosthecochloris aestuarii. Hence, it is necessary to adjust all ingredients (BChl excitation energies and inter−BChl couplings)

for the simulation of the data in refs 12 and 14. This has been achieved in fitting cw-absorption spectra from ref 12.

In utilizing the dissipative multiexciton theory, we chose a way which enables us to describe the electronic (excitonic) states in a satisfactory manner but also allows to account for the coupling to the many vibrational modes present in such pigment−protein complexes. More sophisticated quantum chemical techniques to determine the electronic structure of an antenna complex cause huge numerical efforts, and less can be done to include vibrational modulations of the electronic spectra and interstate couplings (see, e.g., ref 17).

Our approach starts with a simple model for the electronic spectra of the various BChls including the ground state S_0 and the first excited singlet state $S_1(Q_y)$. Since the coupling among those BChls is weak which belong to different monomers of the FMO trimer it suffices to concentrate on the seven BChls of a single monomer. This is a good approximation in particular for femtosecond pump−probe spectra. However, to interpret these types of spectra transitions from the single-exciton states to higher excited states have to be included. The next higher excited states following the single-exciton states are reached via a simultaneous excitations of two BChls leading to the formation of the two-exciton manifold. Alternatively, a higher lying singlet state S_n may be excited. All these excitations are coupled via Coulomb forces. According to the smallest interpigment distance of about 11 Å, Coulomb forces can be described in the approximation of interacting point dipoles.

The delocalization of these excitations is caused by the dipole−dipole coupling and results in the formation of multi-exciton states.[15,16,18−26] There may exist different manifolds, every manifold is characterized by the number of excitations in the complex and splits off into the various exciton levels. In the present case we have $N_{mol} = 7$ BChls in the protein monomer of the FMO-complex. For example, this results in $N_{mol} = 7$ exciton levels in the single-exciton manifold, and in $N_{mol}(N_{mol} + 1)/2 = 28$ exciton levels in the two-exciton manifold. The two-exciton manifold and probably higher exciton-manifolds come into play if nonlinear optical experiments are carried out (compare refs 24 and 26).

The electronic levels of a single BChl as well as the electronic coupling among different BChls are modulated by intramolecular vibrations as well as by the huge amount of vibrational degrees of freedom of the protein matrix. The very slow protein motions, with vibrational periods much larger than any characteristic time of the exciton system, can be accounted for by introducing static disorder (inhomogeneous broadening). The faster low frequency protein vibrations as well as the high frequency intramolecular vibrations are considered as forming a heat bath with temperature T which couples to the electronic degrees of freedom. For the FMO-complex this coupling is thought of to be relatively weak, and not any observation of vibrational coherences has been reported. Hence, a perturbational treatment seems to be appropriate. Such a model easily allows for the description of electronic excitation energy dissipation. Emitting or absorbing vibrational quanta of appropriate energy the exciton may jump to neighboring levels. How probable such processes are depends on the manner the excitonic transition energy fits the range where the spectral density of the vibrations is sufficient large.

In the following section we shortly review the dissipative multiexciton approach (details can be found in ref 16) and specify it to the protein monomer of the FMO-complex of Chlorobium tepidum. The results of simulating the cw-

absorption, pump−probe spectra, and the transient anisotropy are explained in detail in section III.

II. Model and Simulation Technique

A. The Hamiltonian. To obtain a Hamiltonian, which allows for the formation of multiexciton states and includes the coupling to vibrational degrees of freedom, let us start with an expansion with respect to the adiabatic electronic states. These are denoted as $\varphi_{jp} \equiv |jp\rangle$ and belong to a single BChl molecule j at position $\mathbf{R}_j$. For the present purposes it suffices that the electronic quantum numbers p comprise the electronic (singlet) ground-state S_0, the S_1-state, and a higher excited singlet state S_n. The last one is only characterized by its transition energy which should roughly be equal to that for the transition from the ground state to the S_1-state. The basic Hamiltonian obtained in this manner reads

$$H = \sum_{j,p} H_{jp}(Q)|jp\rangle\langle jp| + \tfrac{1}{2}\sum_{i,j}\hat{J}_{ij} - \sum_j \hat{\mu}_j \, \mathbf{E}(\mathbf{R}, t) \quad (1)$$

The first contribution contains the vibrational Hamiltonian $H_{jp} = T(Q) + U_{jp}(Q)$ where $Q = \{Q_\xi\}$ denotes the set of intra- as well as intermolecular vibrational coordinates. According to the complex structure of the antenna system this set cannot be specified in more detail. Instead, we will introduce later on an alternative quantity the spectral density of the vibrational modes, which allows for a description of the coupling of these modes to the excitons. Such a use of a vibrational spectral density is based on the concept of normal modes for the protein environment (see, for example, ref 16). Accordingly, we identify the Q with these normal modes and have to use parabolic potential energy surfaces (PES) $U_{jp}(Q) = E_{jp} - \Delta E_{jp} + \sum_\xi \hbar\omega_\xi(Q_\xi - Q_\xi^{(jp)})^2/4$ for them. E_{jp} is the excitation energy of the electronic state $|p\rangle$ and $\Delta E_{jp} = \sum_\xi \hbar\omega_\xi Q_\xi^{(jp)2}/4$ denotes the polarization energy (polaron shift) defined by the dimensionless displacement $Q_\xi^{(jp)}$ of the PES. Furthermore, ω_ξ is the vibrational frequency of mode ξ.

Details of the geometry of the FMO antenna complex enter the third term of eq 1 which gives the Coulomb interaction between BChl at $\mathbf{R}_i$ and BChl at $\mathbf{R}_j$. Taking the point−dipole approximation it reads $\hat{J}_{ij} = \hat{\mu}_i\hat{\mu}_j/|\mathbf{R}_{ij}|^3 - 3(\hat{\mu}_i\mathbf{R}_{ij})(\hat{\mu}_j\mathbf{R}_{ij})/|\mathbf{R}_{ij}|^5$. The dipole operator includes transitions from S_0 to S_1 and from S_1 to S_n $\hat{\mu}_j = \mathbf{d}_j(S_0 \rightarrow S_1)|jS_1\rangle\langle jS_0| + \mathbf{d}_j(S_1 \rightarrow S_n)|jS_n\rangle\langle jS_1| + hc$. Finally, the fourth term in eq 1) denotes the coupling to the electric field of the external laser pulses which contains in the pump−probe configuration the pump (pu) and the probe (pr) contribution

$$\mathbf{E}(\mathbf{R}, t) = \sum_{s=\text{pu,pr}} \mathbf{e}_s E_s(t) \exp\{i(\mathbf{k}_s\mathbf{R} - \Omega_s t)\} + cc \quad (2)$$

The carrier waves of the two pulses are characterized by their wave vectors $\mathbf{k}_s$ and their frequencies Ω_s. The directions of the linear polarization of the pulses are given by the unity vectors $\mathbf{e}_s$, and the pulse envelopes are denoted by $E_s(t)$. Since the wavelength in the visible region is long compared to the extension of an antenna system, the position vectors $\mathbf{R_j}$ of the BChls have been replaced by a single quantity $\mathbf{R}$ labeling the whole complex.

For the treatment of the ultrafast exciton dynamics in chromophore complexes like the FMO-complex one can choose a representation using single BChl states or delocalized multi-exciton states (eigenstates of the complex). In any case, it is necessary to formulate all rate-expression governing the dissipation in these eigenstates (compare also refs 15, 16, and 27).

Photosynthetic Antenna Systems

J. Phys. Chem. A, Vol. 102, No. 23, 1998 **4383**

Only in this case the correct time asymptotics are obtained which lead to a thermal equilibrium population of the exciton states. Therefore, it is most appropriate to expand the Hamiltonian with respect to the delocalized exciton states. Since all states have to be distinguished with respect to the number of excited BChl we arrange the Hamiltonian eq 1 in such a manner to indicate explicitly the presence of a single excitation in the antenna complex, the presence of two excitations, and so on. A single excitation appears after light absorption in the visible region and is of the amount of the transition energy from the ground to the S_1-state. The state of two of such excitations present at different BChl molecules may become degenerated with the state of a single BChl excited into the S_n-state.

B. Multiexciton States. For every type of excitations one can define delocalized exciton states. Besides the ground state $|0\rangle$ one obtains multiexciton states $|nN\rangle$ with energy spectrum ϵ_{nN}. Here, n counts the number of excitations present in the complex (the number of excitons) and N is the quantum number of the internal state within this n-exciton manifold. These multiexciton states are defined as eigenstates of the exciton part of Hamiltonian eq 1

$$H_{ex} = \sum_{i,p} E_{jp}|jp\rangle\langle jp| + \frac{1}{2}\sum_{i,j}\hat{J}_{ij}(\mathbf{R}_{ij}^{(0)}) \quad (3)$$

The expansion of this quantity using its *eigenstates* reads

$$H_{ex} = \sum_{n,N} \epsilon_{nN}|nN\rangle\langle nN| \quad (4)$$

This exciton Hamiltonian can be calculated if structural data of the antenna system are available as well as the magnitudes of the various excitation energies and transition dipole moments. In the case of Prosthecochloris aestuarii for which the FMO-complex has been originally resolved these data are at hand. For the structural somewhat different complex of Chlorobium Tepidum we fit the cw-absorption spectra of ref 12 to adjust our theoretical model.

The exciton Hamiltonian eq 4 does not depend on any vibrational degree of freedom, what has been indicated in eq 3 by the dependence of the dipole−dipole coupling on a reference distance $\mathbf{R}_{ij}^{(0)}$ between the interacting BChls.

To get the multiexciton expansion of the Hamiltonian eq 1 we use the completeness relation $1 = \sum_{n,N}|nN\rangle\langle nN|$. It follows

$$H = \mathcal{H}^{(0)}|0\rangle\langle 0| + \sum_{n>0}\sum_{M,N}\mathcal{H}^{(n)}(M,N)|nM\rangle\langle nN| + H_{vib} +$$
$$\sum_{m,n}H^{(mn)} \quad (5)$$

Before explaining the first part of this Hamiltonian in more detail we note that H_{vib} describes the vibrational dynamics at the reference configuration of the antenna complex defined for the case at which any electronic excitation is absent (state $|0\rangle$). All terms characterizing transitions among different exciton manifolds (optical excitation and deexcitation) are collected in the last term of eq 5, $H^{(mn)}$. Transitions within a given n-exciton manifold are contained in $\mathcal{H}^{(n)}(M,N) = \delta_{M,N}\epsilon_{nN} + \sum_{\xi}\hbar\omega_{\xi} g_{\xi}^{(n)}(M,N)Q_{\xi}$. The diagonal part gives the energy spectrum ϵ_{nN}, whereas the off-diagonal part follows from the exciton−vibrational coupling. $g_{\xi}^{(n)}(M,N)$ is originated by the linear electron−vibrational coupling defined via the displacement $Q^{(jp)}$ of the BChl PES and a linear expansion of the dipole−dipole coupling with respect to the various Q_{ξ}. Furthermore, a transformation of both expansions into the delocalized multi-

exciton representation is necessary. In contrast to the energy spectrum, the vibrational spectrum and the exciton−vibrational coupling constants $g_{\xi}^{(n)}(M,N)$ are completely unknown for both types of FMO-complexes. They will be defined in an indirect way via reasonable assumptions with respect to the spectral density of the protein vibrations. However, there exists a resonance Raman study of the high-frequency vibrations of the BChls embedded in the FMO complex.[28] Some of these intramolecular vibrational modes in the low-frequency region might influence the exciton relaxation in the FMO-complex especially for larger energetic differences within the exciton manifold as they occur for instance in a direct relaxation from the blue edge of the manifold to the bottom. But for smaller energies the spectral density of the protein vibrations should better fit the energetic range of exciton relaxation. In principle, both cases localized as well as delocalized vibrations of the environment are taken into account by the introduction of a correlation radius of the vibrations as we will see below. The value of the correlation radius will be fitted to the experiment. From this it can be decided whether exciton relaxation is governed by delocalized protein vibrations or localized BChl vibrations.

C. Dissipative Dynamics. The optical spectra measured on the FMO antenna complex are mainly influenced by transitions among the various electronic states of the coupled BChl molecules. Although vibrational coherences, in particular those induced by the protein matrix, have been observed at other complexes, nothing is known on such phenomena for the present system. Hence, it suffices to choose a theoretical description which considers all vibrational degrees of freedom of the protein environment as a passive system, only accepting and dissipating electronic excitation energy. Dissipative quantum dynamics gives the conceptual framework to deal with this type of system. Therefore, we identify the protein environment as a thermal reservoir and the various (delocalized) exciton states as the active (relevant) system.

The method of our choice is the density matrix approach based on the reduced density matrix (RDM) of the multiexciton system. To have a compact notation we abbreviated the multiexciton states $|nN\rangle$ by $|\nu\rangle$ and get the RDM as $\rho_{\mu\nu}(t)$. Starting from the time-dependent statistical operator of the whole exciton−vibrational system the RDM is obtained via a trace operation with respect to the vibrational degrees of freedom. In the following we provide that the RDM obeys the multiexciton variant of the multilevel Redfield equation.[29,30] Its dissipative part reduced to the so-called secular terms[31] reads

$$\left(\frac{\partial}{\partial t}\rho_{\mu\nu}\right)_{|diss} = 2\delta_{\mu\nu}(\sum_{\kappa} R_{\kappa\to\mu}\rho_{\kappa\kappa} - \sum_{\kappa} R_{\mu\to\kappa}\rho_{\mu\mu}) -$$
$$(1 - \delta_{\mu\nu})(\sum_{\kappa}[R_{\mu\to\kappa} + R_{\nu\to\kappa}] + \tilde{R}_{\mu\nu})\rho_{\mu\nu} \quad (6)$$

The Redfield tensor splits off into energy relaxation and (pure) dephasing rates, given as $R_{\mu\to\kappa}$ and $\tilde{R}_{\mu\nu}$, respectively. Since the exciton levels within a given manifold are supposed to lie not equally spaced, the so-called coherence transfer terms[32] do not contribute here. The energy relaxation rates are obtained as

$$R_{\mu\to\nu} = (1 + n(\omega_{mMN}))\,\mathcal{J}(mMN,mMN,\omega_{mMN}) +$$
$$n(-\omega_{mMN})\,\mathcal{J}(mMN,mMN;-\omega_{mMN}) \quad (7)$$

where $n(\omega)$ is the Bose−Einstein distribution, and $\mathcal{J}$ denotes the spectral density. $\mathcal{J}$ is the crucial quantity, which governs the relaxation of excitons. Since the frequency dependence of this quantity is hardly obtainable an ansatz will be used for

reproducing the measured data. To remain sufficient simple and to keep the number of fit parameters as small as possible, we neglect a possible modulation of the dipole−dipole interaction by the protein environment. Hence the exciton−vibrational coupling is caused by the environment induced modulation of the energy levels of the seven BChls only. As already outlined, this coupling is characterized by the displacements $Q_\xi^{(jp)}$ of the PES of BChl j in the electronic state p. A transformation of this coupling into the basis of delocalized exciton states defines the spectral density in the exciton representation. In the case of the one-exciton manifold, which is of main interest for the following, we obtain

$$\mathcal{J}(1MN,1MN;\omega) = \sum_{ij} c_i(1M)c_i(1N)c_j(1M)c_j(1N)\mathcal{J}_{ij}^{(1)}(\omega) \tag{8}$$

The $c_i(1M)$ term denotes the ith component of the Mth one-exciton eigenvector, and the two-site spectral density reads as $\mathcal{J}_{ij}^{(1)}(\omega) = 1/4\sum_\xi \omega_\xi^2 Q_\xi^{(iS_1)}Q_\xi^{(jS_1)}\delta(\omega - \omega_\xi)$. If every pigment couples to localized vibrations only, the two-site spectral density would become proportional to δ_{ij} (that is, it would equal zero if different BChls are considered). On the contrary, if all vibrations are completely delocalized with respect to the protein matrix, $\mathcal{J}_{ij}^{(1)}$ should only weakly depend on i and j. Since for the considered system it seems reasonable to assume the existence of localized as well as delocalized vibrations, we propose the following ansatz

$$\mathcal{J}_{ij}^{(1)}(\omega) = e^{-R_{ij}/R_c} \mathcal{J}_{mol}(S_1,\omega) \tag{9}$$

which interpolates between the two limiting cases. The quantity R_c can be interpreted as a correlation radius of the exciton vibrational interaction. It determines how the modulation of the site energies of different BChls are correlated via protein vibrations. In the limit $R_c \rightarrow 0$, these vibrations should be identified with intramolecular vibrations of the BChls. For the remaining single-molecule spectral density we tested three different forms which qualitatively differ in their high energetic tail. Throughout the simulations we tried short, medium and long tails described by $\exp(-\omega^2/\omega_c^2)$, $\exp(-\omega/\omega_c)$ and $1/(\omega^2 + \omega_c^2)$, respectively. For all three types a satisfying fit of the temperature-dependent linear absorption could be obtained. However, from the investigation of the exciton dynamics it could be concluded that the medium tail spectral density gives best characterization of the exciton vibrational coupling. The full single-molecule spectral density used with medium tail reads

$$\mathcal{J}_{mol}(S_1,\omega) = \hbar G\frac{\omega}{\omega_c^2}e^{-\omega/\omega_c} \tag{10}$$

where $\hbar G$ determines the integral strength and ω_c gives the position of the maximum. For the coupling of the higher excited S_n states to the protein environment, we assume $Q_\xi^{(jS_n)} = \eta Q_\xi^{(jS_1)}$ (In the simulation of pump−probe spectra for simplicity $\eta = 1$ is taken.). In this way the related relaxation rates can be traced back also on $\mathcal{J}_{mol}(S_1,\omega)$ and we obtain for the related spectral density governing exciton relaxation in the two-exciton manifold

$$\mathcal{J}(2MN,2MN;\omega) = \sum_{i>j,k>l} c_{ij}(2M)c_{ij}(2N)c_{kl}(2M)c_{kl}(2N) \times$$
$$[\mathcal{J}_{ik}^{(1)}(\omega) + \mathcal{J}_{il}^{(1)}(\omega) + \mathcal{J}_{jk}^{(1)}(\omega) + \mathcal{J}_{jl}^{(1)}(\omega)] +$$
$$2\eta\sum_{i,k>l} c_{ii}(2M)c_{ii}(2N)c_{kl}(2M)c_{kl}(2N)[\mathcal{J}_{ik}^{(1)}(\omega) + \mathcal{J}_{il}^{(1)}(\omega)] +$$
$$\eta^2\sum_{i,j} c_{ii}(2M)c_{ii}(2N)c_{jj}(2M)c_{jj}(2N)\mathcal{J}_{ij}^{(1)}(\omega) \tag{11}$$

Here the coefficient $c_{ij}(2M)$ of the two-exciton state $|2M\rangle$ describes for $i = j$ how the S_n-state of the ith BChl contributes to the two-exciton state, and for $i \neq j$ the contribution from the simultaneously excited BChls i and j in the S_1 state is considered.

Pure dephasing processes are only of some importance for the line width of the lowest exciton level. Nevertheless, we shortly offer a microscopic picture for them. To do this, one has to include into $H^{(n)}(M,N)$ contributions quadratic with respect to the vibrational degrees of freedom.[25,30] Neglecting again any contribution from the inter-BChl coupling we introduce the on-site coupling constant $k_\xi(jp)$. In this way we obtain, for example, for the dephasing rate of coherences between the ground state $|0\rangle$ and the single-exciton state $|1N\rangle$

$$\tilde{R}_{1n0}\sum_{ij} c_i^2(1N)c_j^2(1N)\phi_1^2(T) +$$
$$\sum_{ij} c_i^2(1N)c_j^2(1N)\exp(-R_{ij}/R_c)\phi_2^2(T) \tag{12}$$

where $\phi_1(T) = \sum_\xi k_\xi(S_1)(1 + 2n(\omega_\xi))$ and $\phi_2(T) = 4\sum_\xi k_\xi^2(S_1)n(\omega_\xi)(1 + n(\omega_\xi))$. Note that we assumed an independence of $\phi_1(T)$ and $\phi_2(T)$ on the BChl index.

D. The Nonlinear Optical Response. As already outlined in some foregoing papers,[25,26] it is of technical advantage in determining the ultrafast optical response if the density matrix is expanded with respect to the carrier waves of the external pump and probe fields (compare also ref 22). We write

$$\rho_{\mu\nu}(t) = \sum_{n_{pu},n_{pr}=-\infty}^{\infty} \sigma_{\mu\nu}^{(n_{pu},n_{pr})}(t)\exp\{i\sum_{s=pu,pr}n_s(\mathbf{k}_s\mathbf{R} - \Omega_s t)\} \tag{13}$$

The appearance of the vector $\mathbf{R}$ indicates that the dynamics of a single complex positioned at $\mathbf{R}$ is concerned. To calculate the macroscopic polarization $\mathbf{P}(\mathbf{R},t)$, which determines the optical signal, it is necessary to sum up the expectation values of the dipole operator $\hat{\mu} = \sum_R \hat{\mu}(R)$ of all complexes contained in the probe volume.

There are two main advantages of the expansion 13. First, the expansion enables one to extract from the overall light-induced polarization wave the particular part $\mathbf{P}_{01}(\mathbf{R},t) = \mathbf{e}_{01}P^{(01)}(t)\exp i(\mathbf{k}_{pr}\mathbf{R} - \Omega_{pr}t)$ (with $n_{pu} = 0, n_{pr} = 1$) which travels in probe−pulse direction. This contribution is needed to calculate the related time-integrated absorption signal of the probe−pulse measured in a pump−probe setup which is given as[33]

$$S_{tot} = 2\Omega_{pr}(\mathbf{e}_{pr}\mathbf{e}_{01})\int dt \, \text{Im}\{E_{pr}(t)P^{(0,1)*}(t)\} \tag{14}$$

The second advantage of the expansion 13 concerns the numerical solution of the RDM equations. Since only the envelopes of the external fields enter these equations, any fast oscillation with the optical periods Ω_{pu}^{-1} or Ω_{pr}^{-1} is absent, making their numerical solution more stable. For the numerical computations, the field envelopes $E_{pu}(t)$ and $E_{pr}(t)$ are taken as real functions of Gaussian shape.

Photosynthetic Antenna Systems

J. Phys. Chem. A, Vol. 102, No. 23, 1998 **4385**

The equations of motion for the expansion coefficients of the RDM read

$$
\frac{\partial}{\partial t}\sigma_{\mu\nu}^{(n_{\mathrm{pu}},n_{\mathrm{pr}})} = -i(\omega_{\mu\nu} - n_{\mathrm{pu}}\Omega_{\mathrm{pu}} - n_{\mathrm{pr}}\Omega_{\mathrm{pr}})\sigma_{\mu\nu}^{(n_{\mathrm{pu}},n_{\mathrm{pr}})} +
$$

$$
\frac{i}{\hbar}\sum_K E_{\mathrm{pu}}(t)\{\langle\hat{\mu}|\hat{\mu}|m+1K\rangle\,\sigma_{m+1K\nu}^{(n_{\mathrm{pu}}+1,n_{\mathrm{pr}})} -
$$

$$
\langle n-1K|\hat{\mu}|\nu\rangle\sigma_{\mu n-1K}^{(n_{\mathrm{pu}}+1,n_{\mathrm{pr}})} + \langle u|\hat{\mu}|m-1K\rangle\,\sigma_{m-1K\nu}^{(n_{\mathrm{pu}}-1,n_{\mathrm{pr}})} -
$$

$$
\langle n+1K|\hat{\mu}|\nu\rangle\,\sigma_{\mu n+1K}^{(n_{\mathrm{pu}}-1,n_{\mathrm{pr}})}\} + \{\mathrm{pu}\leftrightarrow\mathrm{pr}\} + \frac{\partial}{\partial t}(\sigma_{\mu\nu}^{(n_{\mathrm{pu}},n_{\mathrm{pr}})})_{|\mathrm{diss}} \quad (15)
$$

The equations already take notice of the fact that the total dipole operator $\hat{\mu}$ of the antenna complex has only off-diagonal matrix elements with respect to the quantum number of the exciton manifolds. Hence, due to the action of the pump and probe field, neighboring exciton manifolds are coupled and the numbers n_{pu} and n_{pr} are changed also. In general, we therefore get an infinite set of coupled differential equations. However, as discussed at length in ref 26 the relation $n_{\mathrm{pu}} + n_{\mathrm{pr}} = m - n$ among the different indices characterizing $\sigma_{\mu=(mM)\nu=(nN)}^{(n_{\mathrm{pu}},n_{\mathrm{pr}})}$ holds if the rotating wave approximation has been invoked.

Since the probe pulse acts only weakly we include the probe field strength up to a linear approximation (i.e., n_{pr} is limited to the values $\{-1,0,1\}$). Thus, the set of differential equations is closed because n_{pu} is determined by n_{pr} and the exciton quantum numbers m and n. For the latter and in the case of an arbitrary strong pump−pulse we have to include their full range (i.e., in the considered case m and n could take values from 0 (ground state) up to 7 for the 7-exciton manifold). In the following we will restrict ourselves to low pump intensities where exciton−exciton annihilation, which gives nonradiative transitions between higher exciton manifolds,[24] can be neglected. In this low-intensity case it is sufficient to take into account the one-exciton manifold plus a possible polarization between the one and the two-exciton manifold. This restriction is equivalent to an approach based on the third-order nonlinear susceptibility ($\chi^{(3)}$-theory, see, e.g., ref 19 and 22). Hence, m and n are restricted to $\{0,1,2\}$.

We should mention here that an inclusion of non-radiative transitions between the two and the one-exciton manifold (IC process) could lead to an additional broadening of the excited-state absorption. However, to the best of our knowledge, besides a picosecond pump−probe study[34] on the FMO-complex of Prosthecochloris aestuarii, there is no experimental estimation of the IC-coupling constant in the femtosecond region. For clarity, we omit the introduction of a further parameter and neglect IC processes. In the case of the LHC-II we were able to estimate this constant from a fit of the intensity dependence of pump−probe spectra.[24,26] Therefore, similar femtosecond experiments on the FMO-complex would be very helpful to clarify the role of nonradiative transitions and, following from this, of exciton−exciton annihilation.

III. Results

A. Linear Absorption. We start with the investigation of the linear optical response of FMO monomers in the frequency domain and simulate in the following the linear absorption measured by Freiberg et al.[12] on the FMO complex of chlorobium tepidum in dependence on temperature. This calculation goes one step further than standard approaches. These neglect dynamic disorder and take into account static disorder by an inhomogeneous broadening of exciton δ-shaped, so-called stick

spectra which are obtained after diagonalizing H_{ex} (eq 3). Here we have in mind a calculation of realistic homogeneous spectra which are then also convoluted with an inhomogeneous distribution function. Concerning static disorder it is most adequate to introduce an inhomogeneous distribution of site energies and diagonalize H_{ex} for many different realizations of disorder. But such an approach would be numerically too time-consuming here because much effort is necessary to optimize the microscopic parameters which will be specified below. In a recent paper,[35] the appropriate treatment of static disorder was investigated for the linear absorption and circular dichroism of the FMO-complex of Prosthecochloris aestuarii. From this study we have learned that the error by convoluting the stick spectra instead of a random generation of site energies is in ordinary linear absorption neglectable but for the circular dichroism spectra remarkable. Since we expect our spectra to be broadened partly homogeneously, we may well expect the error caused by the present treatment of static disorder even smaller than in ref 35.

Another advantage of the calculation of homogeneous spectra lies in the fact that this enables us to study also the temperature dependence of optical spectra. In this way we hope to extract from the simulations in the frequency domain the parameters of the protein dynamics which influence exciton relaxation. The obtained set of parameters will be tested afterwards in the time domain by fitting ultrafast pump probe spectra measured on chlorobium tepidum.

Since this FMO-complex has a microscopic structure slightly different from that of Prosthecochloris aestuarii, which has been treated within the standard model, another reason for a recalculation of the linear absorption is to achieve a fine-tuning of the parameters determining the exciton spectrum.

To get the desired exciton spectrum we start with the microscopic data of chlorobium tepidum[7] and determine the intermolecular Coulomb interactions between the pigments within the point dipole approximation (see the foregoing section). The directions of Q_y dipole moments were taken along the $N_I - N_{III}$ axis of the BChls which correspond to the N_B-N_D axis in the Brookhaven Protein Data Bank nomenclature. Besides the known geometry the two crucial quantities entering the calculation of the interactions between pigments are the Q_y dipole strength of the BChls and the relative dielectric constant ϵ_r of the protein environment. In a recent paper[11] on optical steady-state spectra of the FMO-complex of Prosthecochloris aestuarii a screening of the Coulomb interaction by $1/\epsilon_r$ has been taken into account and for $\epsilon_r = 2.4$ the best simulations have been obtained. However, as it has been brought into discussion in ref 36, in addition to the screening one has to consider also local field corrections of the dipole moments what gives altogether a correction factor of $1/\epsilon_r((\epsilon_r + 2)/3)^2$. Thus for $\epsilon_r = 2.4$ the Coulomb interaction would be reduced only by a factor 0.9. We follow[36] and take $\epsilon_r = 1$. In comparison to monomeric BChla in solution, for which for instance in acetone a Q_y dipole strength of 41 D^2 was measured,[37] it is assumed that due to the protein environment in the FMO-complex the Q_y transitions of the BChls exhibit an increased dipole strength (at the expense of other transitions in the four orbital model). Values between 50 and 70 D^2 (see for instance the references cited in ref 11) are commonly used. Here we will take a dipole strength of 51 D^2 which is close to the value 50.8 D^2 suggested by Fenna.[8] In Table 1 the resulting Coulomb interactions for FMO-monomers of chlorobium tepidum in point−dipole approximation are listed.

TABLE 1: Calculated Dipole−Dipole Interactions in FMO-Monomers of *Chlorobium tepidum* in Units of cm⁻¹. Used Dipole Strength for the Q_y Transition of the BChls $|d_{S_0 \to S_1}|^2 = 51$ D²

BChl	2	3	4	5	6	7
1	−187	11	−9	11	−14	−7
2	49	14	3	23	1	
3	−111	−1	−16	32		
4	−122	−33	−101			
5	164	−4				
6	53					

In order to determine the linear absorption spectra the external field (eq 2) is reduced to a cw-excitation with a weak probe beam with frequency Ω and amplitude $\mathbf{E}_\Omega$. Since $\mathbf{E}_\Omega$ is time-independent, the expansion coefficients $\sigma^{(n_{pr})}$ of the RDM are time independent, too. Following from this, the equations of motion (eq 15) are reduced to a set of algebraic equations which have to be solved in the limit of weak excitation. Hence, there is no depopulation of the ground state (i.e., we have $\rho_{00}(t)=1$).

The linear absorption can be easily deduced from the frequency dispersed signal $S_{tot}(\Omega) = 2\Omega Im\langle \mathbf{E}_\Omega^* \mathbf{P}_\Omega^{*(1)}\rangle_{orient}$ of S_{tot} (eq 14). Here, $\langle...\rangle_{orient}$ denotes an orientational averaging, and $\mathbf{P}_\Omega^{(1)}$ is the envelope of the light-induced polarization wave traveling in the probe−pulse direction. It is obtained from the RDM as $\mathbf{P}_\Omega^{(1)} = \sum_N \mathbf{d}_{1N0}\sigma_{1N0}^{(n_{pr=1})}$. The dipole matrix element for the optical transition from the ground state to the Nth single-exciton state reads $\mathbf{d}_{1N0} = \langle 1N|\sum_j \hat{\mu}_j|0\rangle$. As a result, the absorption coefficient is obtained as a superposition of seven Lorentzians corresponding to the seven possible single-exciton transitions i.e., $\alpha(\Omega) = \sum_N A_{1N}(\Omega - \omega_{1N0})$. The single line follows as (n_{FMO} is the volume density of the complexes)

$$A_{1N}(\Omega - \omega_{1N0}) = \frac{2\pi\Omega}{\hbar c}n_{FMO}|\mathbf{d}_{1N0}|^2\frac{\gamma_{1N}}{(\Omega - \omega_{1N0})^2 + (\gamma_{1N}/2)^2}$$

(16)

The exciton line widths $\gamma_{1N}/2$ are given by the (temperature dependent) energy relaxation and the pure dephasing rates as $\gamma_{1N}/2 = \sum_M R_{1N \to 1M} + \tilde{R}_{1N0}$. Finally, to take into account static disorder we assume a Gaussian distribution function $f(\omega_{1N0} - \bar{\omega}_{1N0})$. It broadens the exciton levels $\bar{\omega}_{1N0}$ which correspond to a reference configuration. The introduction of a single distribution for all seven exciton transitions has been done to restrict the fit parameters to an acceptable amount. The measured linear absorption spectrum $\alpha(\Omega)$ then follows as a sum of convolutions $\alpha(\Omega) = \sum_N \int d\omega_{1N0}f(\omega_{1N0} - \bar{\omega}_{1N0})A_{1N}(\Omega - \omega_{1N0})$.

Besides the site energies E_{jS_1}, together with the mutual Coulomb interaction among the BChls, the inhomogeneous line width σ_{inh}, the spectral density $\mathscr{J}_{mol}(S_1,\omega)$ and the correlation radius R_c of the BChl−protein coupling will influence the shape of the spectra. According to this approach, there are 11 free parameters determining the linear absorption spectrum, namely the seven site energies E_{jS_1}, the inhomogeneous width σ_{inh}, and the parameters $\hbar G$, ω_c, and R_c characterizing the pigment−protein coupling (compare eqs 9 and 10). To find the optimal parameter set, a standard Simplex optimization algorithm[38] has been used. This procedure was applied to search for the minimum of the mean-square discrepancy between the experimental and the theoretical spectra. The program has been written in such a way that the best possible simultaneous fit of the linear absorption at two different temperatures (5 and 107 K) is found. In this way we avoid to introduce additional temperature dependence via a temperature dependence of the
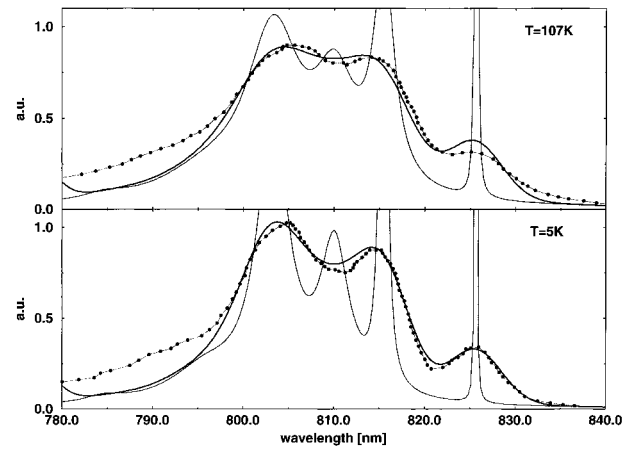

Figure 1. Linear absorption at different temperatures. The calculated spectra for the optimized parameter set (see text and 2nd row of Table 2) are drawn as thick lines. Thin lines show the calculated homogeneous spectra (i.e., before convoluting with a Gaussian distribution function). The points represent the experimental values measured by Freiberg et al.[12]

TABLE 2: Optimized Site Energies E_{jS_1} of the Seven BChls ($j = 1...7$) in the FMO-Monomers of Chlorobium Tepidum (This Work) and of the FMO-Monomers of *Prosthecochloris aestuarii* from Former Works. The Abbreviations OKT and PS Refer to Two Different Sample Preparations

BChl	E_{jS_1} [eV]				
	this work	ref 11	ref 10	ref 9 (OKT)	ref 9 (PS)
1	1.589	1.527	1.542	1.580	1.556
2	1.538	1.542	1.545	1.553	1.537
3	1.508	1.504	1.540	1.548	1.518
4	1.551	1.527	1.538	1.543	1.534
5	1.549	1.558	1.535	1.550	1.589
6	1.541	1.544	1.520	1.527	1.532
7	1.557	1.541	1.544	1.508	1.555

TABLE 3: Single-Exciton Energies ϵ_{1N}, Dipole Strength of the Related Transitions from the Ground State in Units of the Q_y Dipole Strengths of the BChls, and Temperature Dependent Homogeneous Line Widths $\gamma_{1N}(T = 5$ and 107 K) of the Single-Exciton Levels

N	ϵ_{1N} [eV (nm)]	$|d_{1N0}|^2$ [51 D²]	$\gamma_{1N}(T = 5$ K) [cm⁻¹]	$\gamma_{1N}(T = 107$ K) [cm⁻¹]
1	1.502 (825.6)	0.53	0.59	1.58
2	1.520 (815.4)	1.23	5.23	20.42
3	1.531 (810.1)	1.27	29.47	43.11
4	1.544 (803.2)	2.57	32.66	56.05
5	1.558 (795.8)	0.69	75.58	98.93
6	1.580 (784.7)	0.08	42.72	46.72
7	1.598 (775.6)	0.62	0.92	0.97

fit parameters. Now, temperature only enters via the homogeneous line widths γ_{1N}. In Figure 1 the experimental spectra at 5 and at 107 K are shown in comparison to the theoretical spectra obtained with the optimized set of site energies given in the second row of Table 2. In addition, the homogeneous spectra are also shown as thin lines. The obtained homogeneous line widths of the different transitions $|0\rangle \to |1N\rangle$ depend on the exciton quantum number N as well as on temperature (compare Table 3). At 5 K, the transition to the lowest exciton level occurring at 825.6 nm exhibits the smallest line width, because at this temperature no energy transfer occurs to higher exciton states. The homogeneous line width of this transition is determined by the pure dephasing which has been chosen independent of temperature and small compared to the linear electron−vibrational coupling constant (i.e., small with respect
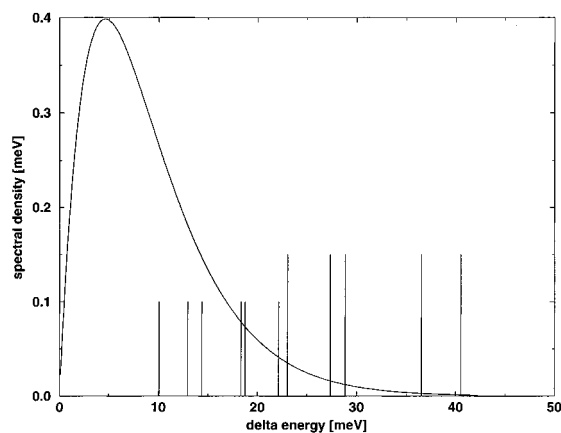
Photosynthetic Antenna Systems

J. Phys. Chem. A, Vol. 102, No. 23, 1998 **4387**

Figure 2. Spectral density of the pigment−protein coupling according to eq 10 with optimized parameters $\hbar G = 5.0$ meV and $\hbar \omega_c = 4.6$ meV (37 cm^{-1}). As vertical lines the position of those exciton transition frequencies are labeled, at which the spectral density enters the exciton dynamics. Short lines represent energetic differences between neighboring (i.e., 11−12, 12−13, ..., 16−17) one-exciton states. Longer lines are positioned at the energy differences between the next but one neighboring levels (i.e., 11−13, 12−14, ..., 15−17).

to the integral strength $\hbar G$ of the spectral density). Therefore we use $\hbar \phi_1^2 = 0.1$ meV and $\phi_2 = 0$.

At higher temperatures upward energy transfer from the lowest exciton state occurs and a broadening of this line as well as the other lines appears. This becomes obvious for the absorption spectrum at 107 K. Looking on the measured spectra there seems to be a temperature-dependent redistribution of oscillator strength between the two absorption peaks at 815 and 803 nm. However, the spectra calculated without inhomogeneous broadening demonstrate that this observation is related to the temperature dependent broadening of an intermediate transition occurring at 810 nm. Since this excitation lies energetically slightly closer to the low energetic absorption maximum at 815 nm the latter is risen relative to the other maximum at 803 nm by the broadening.

As a general trend we observe for the homogeneous line widths an increase with increasing quantum number of the one-exciton state (one exception is the highest one-exciton state—compare also Table 3). Moving to higher energies, the absorption is thus determined more and more by homogeneous broadening. This is determined by both the spectral density and the correlation radius of the exciton vibrational coupling. From our fit routine an optimal correlation radius $R_c = 21$ Å was determined. This value is in the order of the extension of the whole FMO-monomer what can be understood as a proof for the existence of delocalized exciton vibrational interaction. Thus we can identify the vibrations which are responsible for exciton relaxation with vibrations of the protein body the pigments are embedded in. However, in addition to the protein vibrations it might be worth taking into account also low-frequency parts of localized BChl vibrations. This would open new dissipation channels especially for higher energies as they occur for instance in a relaxation from the top of the one-exciton manifold directly to the bottom. This would broaden the optical transition to the highest one-exciton state and should improve the simulation especially for short wavelengths. We will leave this for future work and concentrate here on the relaxation from the states energetically at the maximum of the absorption at 803 nm to the bottom of the manifold at 825 nm.

Transitions among the different exciton states and thus homogeneous broadening are determined by the spectral density of the pigment−protein coupling. In Figure 2 the spectral
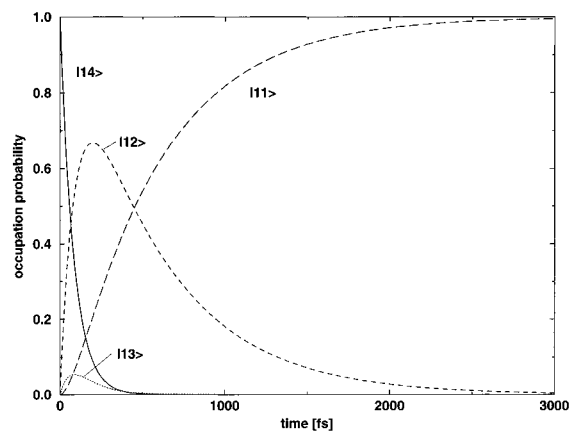

Figure 3. Relaxation in the single-exciton band, calculated for an initial population of the fourth exciton state, $\rho_{1414}(t = 0) = 1$, using the parameters of the linear absorption fit.

density is shown, characterized by two parameters which were obtained from the optimization procedure as $\hbar G = 5.0$ meV for the integral coupling strength and $\hbar \omega_c = 4.6$ meV (37 cm^{-1}) for the peak position of the spectral density. The latter is in nice agreement with hole burning studies on the FMO-complex of Prosthecochloris aestuarii,[39] where a mean frequency of low-frequency protein vibrations of 30 cm^{-1} was found. The optimized inhomogeneous width of 101 cm^{-1}, however, is much larger than the 20 cm^{-1} estimated in ref 39. But in general, values around 70 cm^{-1} are common in photosynthetic antenna complexes.

Also drawn in Figure 2 are the transition frequencies ω_{1MN} between nearest-neighbor exciton levels (ω_{1MM-1}, thin vertical lines) and between next but one levels (ω_{1MM-2}, longer lines). Since the value of the spectral density at the frequencies of the transitions between the exciton states within one manifold determines the exciton relaxation rates, the shape of the spectral density gives a rough view on exciton relaxation. From Figure 2 we can conclude that the excitons preferably relax step by step down the ladder of exciton states. But also a relaxation between next but one neighboring states is possible but with lower probability, since the spectral density is smaller for the related transition energies. This may explain why the high energetic transitions are broadened stronger than the low-energetic ones. Simply there are more possible states to relax to what shortens the lifetime and broadens the level.

To illustrate this relaxation the density matrix has been propagated in the absence of external fields, for a temperature of 20 K and an artificially generated initial excitation. Since it will be important for the pump−probe spectra discussed in the next section we assume for simplicity that at time zero all occupation probability is in the fourth one-exciton state (i.e., $\rho_{1414}(t = 0) = 1$). In Figure 3 the exciton dynamics is shown. As it could be concluded already from the spectral density, the exciton relaxes step by step down to the bottom of the manifold, which is reached after about 2 ps. Also we see a relaxation between next but neighboring levels, for instance between $|14\rangle$ and $|12\rangle$. In the next section the dynamics of exciton will be studied under realistic excitation conditions.

We want to finish our investigations in the frequency domain by comparing different approaches for the calculation of linear absorption. In particular we will see how important a realistic model for the homogeneous absorption lines of the FMO-complex is. In Figure 4 the approach of this work is compared with a case for which the homogeneous line width has been neglected (dashed line) and with another simulation in our model
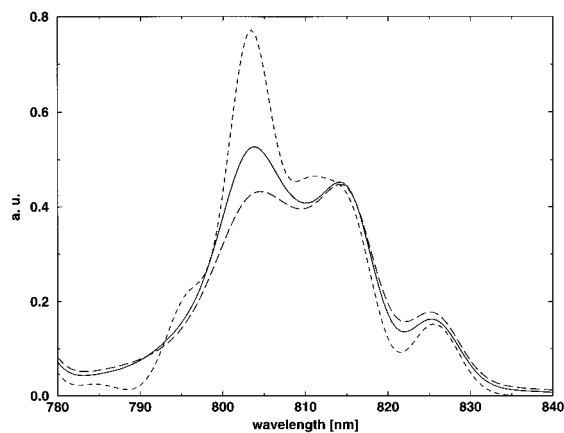
Figure 4. Simulation of the linear absorption at 5 K using different approaches and the parameter set of Figure 1. Solid line: same as in Figure 1. Dashed line: standard approach (i.e., neglecting the homogenous line widths). Long dashed line: present approach but assuming localized exciton−vibrational coupling (i.e., $R_c \rightarrow 0$).

but assuming localized vibrations (i.e., $R_c \rightarrow 0$ (long dashed line)). Especially at a shorter wavelength ($\lambda < 815$ nm), where the homogeneous broadening is strong, there are considerable deviations from our approach which go in opposite directions for the two alternative cases considered here. One may conclude from this that taking a smaller correlation radius of the exciton−vibrational interaction increases the homogeneous line width and therefore should accelerate exciton relaxation.

We summarize that both points (i) taking into account dynamic disorder and (ii) the introduction of a correlation radius for the vibrations proofed to be important for the interpretation of the measured linear absorption and its temperature dependence. If we look again at Table 2 where besides our optimized site energies of the FMO monomers of Chlorobium tepidum the determined site energies of Prosthecochloris aestuarii from former studies are also shown, we see that, in spite of the precisely known microscopic structure, very different results have been obtained. Clearly this indicates the difficulties in modeling such a complex system.

B. Pump−Probe Signal. Next, we demonstrate that the parameters obtained from the fit of the linear absorption can be also used to simulate ultrafast pump−probe spectra. To do this, we concentrate on the measurements of Freiberg et al.[12] carried out at the FMO-complex of Chlorobium tepidum. To simulate these measurements it is necessary to fix two additional parameters which concern the higher excited BChl S_n states. From nonlinear measurements on BChl in solution,[40] it is known that the monomeric excited-state absorption is located around 100 cm^{-1} to the blue of the $S_0 \rightarrow S_1$ transition. We also take this value in our calculations what reduces the number of additional parameters to one namely the dipole moment $\mathbf{d}_j(S_1 \rightarrow S_n) = \mathbf{e}_j d_{S_1 \rightarrow S_n}$ of the intramolecular excited state absorption, where the unit vector $\mathbf{e}_j$ gives the direction of the dipole moment of the BChl at site j and we have taken the same dipole strength for all BChls. For simplicity we assume also that these dipole moments are parallel to the Q_y dipole moment of the BChls (i.e., $\mathbf{d}_j(S_1 \rightarrow S_n) = d_{S_1 \rightarrow S_n}/d_{S_0 \rightarrow S_1}\mathbf{d}_j(S_0 \rightarrow S_1)$. The ratio of the magnitude of dipole moments $d_{S_1 \rightarrow S_n}/d_{S_0 \rightarrow S_1}$ will be fitted in the calculation of pump−probe spectra. Since all the other parameters were fixed before we are able to study the role of intramolecular excited-state absorption for the nonlinear optical response of the FMO complex.

To determine the differential absorption measured in a pump−probe setup, it is necessary to start from the following relation

$$\frac{\Delta\alpha}{\alpha_0} = \frac{S_{tot}(\mathbf{E}_{pu}, \mathbf{E}_{pr}, \tau) - S_{tot}(\mathbf{E}_{pu} = 0, \mathbf{E}_{pr})}{S_{tot}(\mathbf{E}_{pu} = 0, \mathbf{E}_{pr})} \quad (17)$$

Here, $S_{tot}(\mathbf{E}_{pu}, \mathbf{E}_{pr}, \tau)$ is the time-integrated absorption signal of a weak probe−pulse centered at a delay τ after the action of a strong pump pulse (see eq 14). $S_{tot}(\mathbf{E}_{pu} = 0, \mathbf{E}_{pr})$ denotes the linear absorption measured by the probe pulse alone. An orientational averaging with respect to all possible orientations (of the isolated FMO-complexes dissolved in solution) has been incorporated into the definition of both quantities. Here, this averaging has been carried out numerically. The pump and the probe-field polarization are taken at the magic angle (54.7°). In accordance with the experiment, both pulses have a pulse width (fwhm) of 150 fs, and the pump pulse acts at 803 nm. The dynamics of the system is probed by the weak probe−pulse at 803, 815, and at 825 nm where the exciton states $|14\rangle$, $|12\rangle$, and $|11\rangle$, respectively, are located. According to the intermediate strength of inhomogeneous broadening we neglect this effect in determining the pump−probe spectra.

In Figure 5 the calculated spectra are shown in comparison to the experimental signals. The computations reproduce the behavior of the measured spectra very well. For short delay times and for all probe wavelengths the differential absorption signal falls on a femtosecond time scale reflecting the pump pulse-induced ground-state bleaching and stimulated emission. This is followed by a 500 fs rise of the probe pulse signal at 803 nm, a 2 ps rise at 815 nm, and a 2 ps decrease for $\lambda_{pr} = 826$ nm. To see how these signals correlate with the relaxation of excitons in Figure 6 the (orientational averaged) level populations of one-exciton states are shown. Due to the finite width of the pump pulse it is energetically broad enough to excite besides the resonant transition to the state $|14\rangle$ also partly the states $|13\rangle$ and $|12\rangle$. However, from a comparison to the case of an artificially created excitation of $|14\rangle$ as it was investigated in the end of last section (see Figure 3), we see that there is a relaxation $|14\rangle \rightarrow |12\rangle$ already on the time scale of the pump pulse width. This explains the slightly delayed femtosecond decrease of the probe signals at 815 nm after the signal at 803 nm which instantaneously follows the pump pulse (The deviations between experimental data and simulations for negative delay times may be caused by different pulse shapes). Stimulated emission from the lowest exciton state at 826 nm occurs due to exciton relaxation into this state. This relaxation takes about 2 ps as it can be seen in Figure 6 in full agreement with the 2 ps fall of the probe pulse signal at 826 nm in Figure 5. Moreover the 500 fs rise time of the 803 nm signal and the 2 ps rise of the 815 nm signal directly correlate to the depopulation of the exciton levels $|14\rangle$ and $|12\rangle$, respectively, reflecting the decay of stimulated emission from these levels. After about 3 ps the pump−probe signal becomes quasi stationary for all probe wavelengths, indicating that the relaxation within the one−exciton manifold is finished.

However, the pump−probe signal is also influenced by excited state absorption between the one- and the two-exciton manifold. This contribution to the optical response of the aggregate proofs to be sensitive to intramolecular excited-state absorption of the BChls as will be shown now. In Figure 7 the pump−probe signal for the optimal ratio of dipole moments $d_{S_1 \rightarrow S_n}/d_{S_0 \rightarrow S_1} = 0.5$, which was used to simulate the pump probe signal in Figure 5, is shown together with simulations for dipole moment ratios of 0.25 and 0.75. The latter two clearly differ from the first what enables us to state that it is possible to extract this intramolecular parameter of the BChl embedded in the FMO protein from our simulation. Note that all the other parameters were fixed already from the simulation of linear absorption.
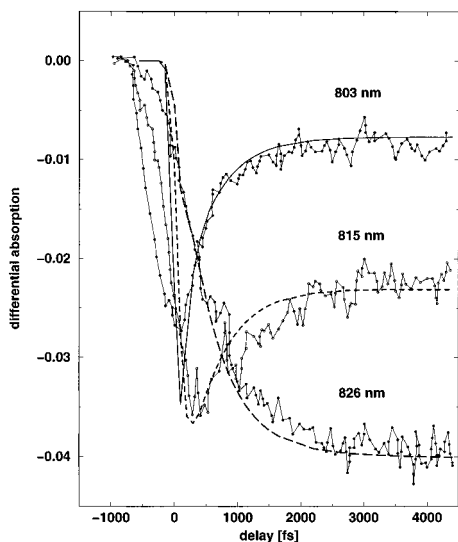
$$d_{S_1 \to S_n} / d_{S_0 \to S_1}$$

Figure 5. Simulation of the 15 K two-color pump−probe experiments of Freiberg et al.[12] (curves with circles) at a pump wavelength of 803 nm and for different probe wavelengths. Solid curve: $\lambda_{pr} = 803$ nm. Dashed curve: $\lambda_{pr} = 815$ nm. Long dashed curve: $\lambda_{pr} = 826$ nm.
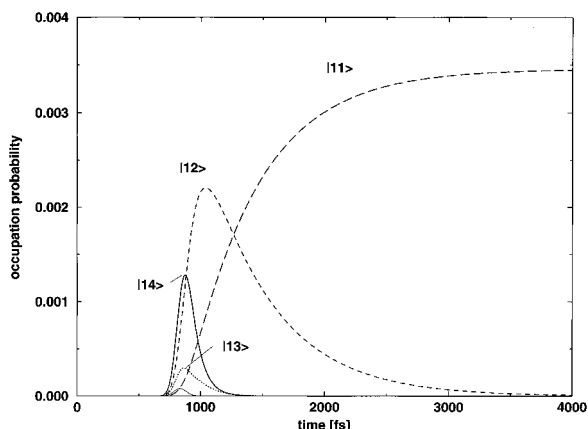

Figure 6. Level population in the one-exciton manifold after excitation with a 150 fs pump pulse acting at $\lambda_{pu} = 803$ nm. Excitation corresponds to that taken in the measurements of the ultrafast pump probe spectra (Figure 5).

As in the case of linear absorption also the temperature dependence of pump−probe spectra can be described within our approach as it is shown in Figure 8 for the simulation of a two color pump probe experiment from ref 12 at $T = 20$ K and $T = 160$ K. As in Figure 5 the pump pulse acts at 803 nm, and the exciton relaxation is probed at the bottom of the one-exciton manifold at $\lambda_{pr} = 825$ nm. With increasing temperature, exciton relaxation gets faster, resulting in a steeper decline of the signal at 160 K, where the stationary value is reached after 1 ps whereas it takes 2 ps at 20 K. Since at higher temperatures higher one exciton states are thermally populated after relaxation, excited-state absorption starting from these states to the two-exciton manifold rises the stationary value of the pump−probe signal.

C. Anisotropy of the Pump−Probe Spectra. Since the vector character of the external field has been taken into account, we can calculate the anisotropy of the pump−probe signal defined as

$$r(\tau) = \frac{\Delta\alpha_{\parallel} - \Delta\alpha_{\perp}}{\Delta\alpha_{\parallel} + 2\Delta\alpha_{\perp}} \quad (18)$$

Here, $\Delta\alpha_{\parallel}$ ($\Delta\alpha_{\perp}$) is the differential absorption for parallel

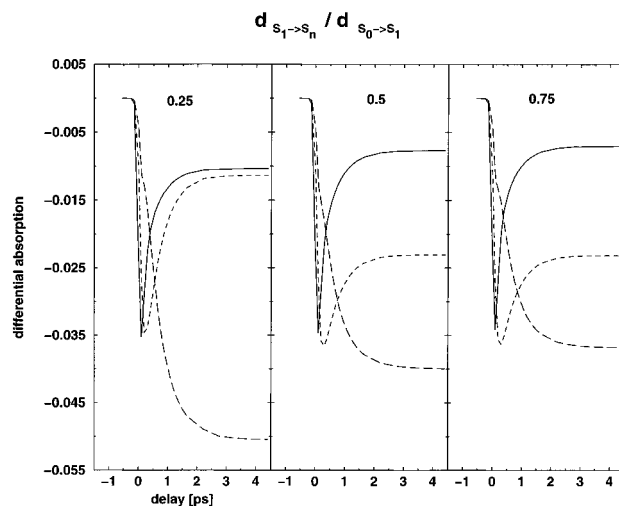**Figure 7.** Variation of ultrafast pump−probe spectra of Figure 5 with changing intramolecular excited state absorption, $d_{S_1 \to S_n}/d_{S_0 \to S_1} = 0.25$ (left), 0.5 (middle), and 0.75 (right).
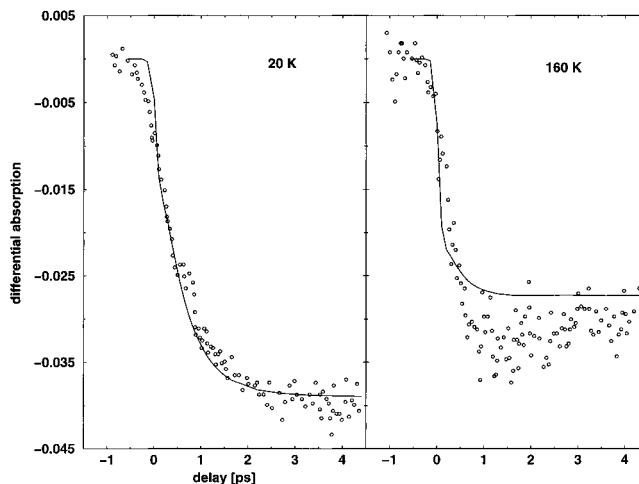

Figure 8. Two-color pump−probe spectra at two different temperatures. Pump wavelength at 803 nm, probe wavelength at 825 nm.

(perpendicular) polarized pump and probe pulses, and τ denotes the delay between the pulses. Of particular interest is the value of the anisotropy at zero delay, which takes the value 0.4 for randomly orientated isolated two-level systems. In the case of a multilevel system this initial value of the anisotropy may become larger than 0.4. A multilevel system may be created, for instance, by the interaction between two-level systems as considered in ref 41, or simply it might be represented by a molecule having two optically allowed transitions with different polarizations. The latter was investigated for degenerated excited levels in ref 42 and for the case in which the molecule exhibits excited state absorption between the first and a higher excited state in ref 43. Considering the FMO-complex, we have a mixture of all the above-mentioned cases. There are several different polarized transitions between the ground state and the one-exciton manifold, and excited state absorption to higher exciton manifolds may take place also.

In a recent study by Savhikin et al.[14] the transient anisotropy was measured at 19 K on trimers of Chlorobium tepidum and presented together with simulations of the initial anisotropy $r(0)$. However, since there were no parameters available the authors used the site energies and Coulomb interactions determined for *Prosthecochloris aestuarii* in ref 9 (see Table 2 (OKT)) for their simulations. We are now in the position to remove this inconsistency by taking our parameters from the fit of the linear
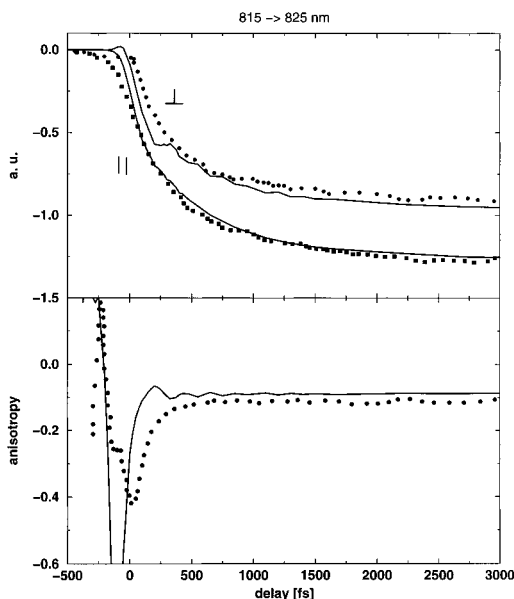
Figure 9. Two-color anisotropy at 19 K, pump wavelength at 815 nm, probe wavelength at 825 nm. Top: Measured pump probe signals for parallel (squares) and perpendicular (circles) polarized pump and probe pulses in comparison to the theoretical curves (full lines). Bottom: resulting anisotropy. Experimental data: circles. Theory: full line. Experimental data were taken from Savhikin et al.[14]
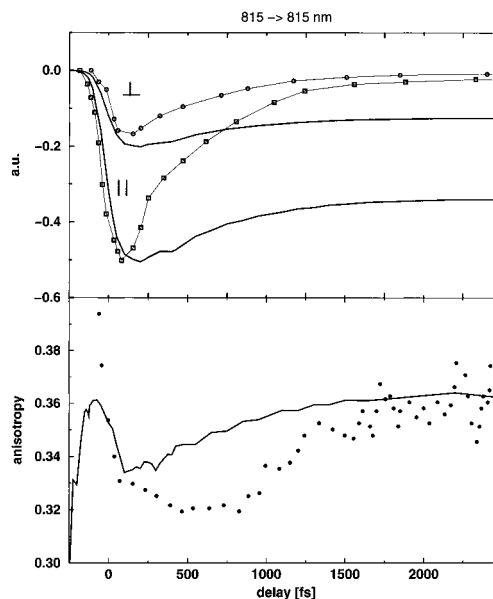

Figure 10. One-color anisotropy at 19 K, pump and probe wavelength at 815 nm. Top: Measured pump−probe signals for parallel (thin line with squares) and perpendicular (thin line with circles) polarized pump and probe pulses in comparison to the theoretical curves (full lines). Bottom: resulting anisotropy. Experimental data: circles. Theory: full line. Experimental data were taken from Savhikin et al.[14]

absorption and the isotropic pump−probe spectra of Chlorobium tepidum from the previous sections. (Note that also intramolecular excited state absorption is taken into account.) Moreover, since we consider dynamic fluctuations of the BChl energies, it is possible to look also on the time evolution of the anisotropy and we may ask how this can be explained by the relaxation of excitons. In Figure 9 the anisotropy is shown together with the pump probe signals for a pump wavelength at 815 nm and $\lambda_{pr} = 825$ nm. The pump−probe curves obtained with parallel and perpendicular polarizations of pump and probe pulse very nicely resemble the experimental data, and also, the resulting anisotropy is in very good agreement with the experiment. Strong variations of the anisotropy for negative delay times and overlapping pump and probe pulses are caused by coherent processes as discussed in detail for three level systems in ref 43. For positive delay times the theoretical and experimental anisotropy remain essentially constant at ≈ -0.1. However, a closer look at the theoretical curve reveals a low amplitude oscillation of the signal for delay times < 1000 fs. The period of this oscillation is about 220 fs what corresponds to an energetic difference $2\pi\hbar/220$ fs ≈ 19 meV occurring between the two lowest exciton states at 815 and 826 nm. Due to the finite pulse width (fwhm = 150 fs) the pump pulse acting at 815 nm is spectrally broad enough to excite also the lowest exciton state directly however with much lower probability. Due to this coherent excitation, a quantum beating of the stimulated emission starting from these two levels modulates the anisotropy with a time constant that corresponds to the energy difference of the two involved transitions. Because of dephasing introduced here by the relaxation of excitons the pump pulse induced coherences will be destroyed and the quantum beats in the anisotropy disappear.

Shifting the pump pulse energetically between the two states should increase the spectral overlap to the lowest state and therefore increase the effect. In fact in ref 14 it was mentioned that changing the pump wavelength leads to strong oscillations of the measured anisotropy.[44] Moreover the experimental observed oscillations are dominated also by a 220 fs period. This

is a further nice proof of the capability of our approach and it may justify the neglect of inhomogeneous broadening as done her for the calculation of the pump−probe spectra. If the inhomogeneous broadening were strong it would lead to a destructive interference of the quantum beats, thus the latter should not be observable.

Finally we want to see how exciton relaxation manifests in the one color anisotropy pumped and probed at 815 nm. The simulation are shown together with the experimental data of ref 14 in Figure 10. In contrast to the two-color case, now the pump−probe spectra only qualitatively fit the experiment. In agreement with the experiment we obtain also a femtosecond decrease of the signals for parallel and perpendicular polarized pump and probe pulse and a following 2 ps rise to stationary values. The latter, however, differ remarkable from the experimental values. It is astonishing, therefore, that the resulting anisotropy fits well the experimental finding (i.e., starting at $r(0) = 0.35$ followed by a fs decrease we see that exciton relaxation manifests itself in the 2 ps rise of the anisotropy, which afterwards reaches its stationary value of ≈ 0.36.

IV. Conclusions

A dissipative multiexciton model has been introduced which is capable for a consistent description of experiments on oligomer photosynthetic antenna systems in the frequency and in the time domain. Details of the exciton relaxation within the single- and the two-exciton band could be described in using a particular type of protein spectral density. This quantity combines the density of states of the protein vibrations and the distribution of coupling strength to the multiexciton system. Models for the spectral density which account for localized as well as delocalized vibrations in the antenna system have been discussed.

The approach could be successfully applied to the FMO-complex of chlorobium tepidum. We reproduced the temperature dependence of the linear absorption and could simulate ultrafast pump−probe spectra together with the transient ani-

Photosynthetic Antenna Systems

J. Phys. Chem. A, Vol. 102, No. 23, 1998 **4391**

sotropy measured by Freiberg et al.[12] and Savhikin et al.,[14] respectively. A fit of the linear absorption also measured by Freiberg et al.[12] has been used to fix the microscopic parameters like the site energies, the inhomogeneous broadening, the spectral density, and the correlation radius of the exciton vibrational coupling. The latter has been introduced to characterize how the modulations of the site energies of different BChls are correlated via protein vibrations.

Based on these parameters it was possible to reproduce two color ultrafast pump−probe spectra pumped at 803 nm and probed at three different wavelengths. In the fit of the pump−probe spectra one additional parameter concerning the dipole moment of intra molecular excited state absorption of the BChls embedded in the FMO protein could be determined.

Finally the strength of the present approach could be demonstrated in the simulation of the one and two color transient anisotropy recently measured by Savhikin et al.[14] In one of the spectra excitonic quantum beats have been found.

Our theory demonstrates that it is possible to use the exciton spectrum as a probe for measuring the shape of the protein spectral density. Either by simulating frequency-domain data (cw-absorption) or time-domain data (femtosecond pump-probe spectra) one can construct the global frequency dependence of the spectral density.

The present approach should be considered as a reference case for more sophisticated studies which will be done in the future. These concern in particular an improvement of the description of disorder. The inclusion of the rather weak intermonomer coupling within the FMO trimer may also improve the simulations presented here.

References and Notes

(1) Deisenhofer, J.; Epp, O.; Miki, K.; Huber, R.; Michel, H. *Nature* **1985**, *318*, 618.

(2) Kühlbrandt, W.; Wang, D. N.; Fujiyoshi, Y. *Nature* **1994**, *367*, 614.

(3) McDermott, G.; Prince, S. M.; Freer, A. A.; Hawthornthwaite-Lawless, A. M.; Papiz, M. Z.; Cogdell, R. J.; Isaacs, N. W. *Nature* **1995**, *374*, 517.

(4) Sundström, V.; Pullerits, T.; van Grondelle, R. In *Femtochemistry and Femtobiology*; Sundström, V., Ed.; World Scientific: Singapore, 1997.

(5) Fenna, R. E.; Matthews, B. W. *Nature* **1975**, *258*, 573.

(6) Tronrud, D. E.; Schmid, M. F.; Matthews, B. W. *J. Mol. Biol.* **1986**, *188*, 443.

(7) Li, Y. F.; Zhou, W.; Blankenship, R. E.; Allen, J. *J. Mol. Biol.* **1997**, *271*, 456.

(8) Pearlstein, R. M. *Photosynth. Res.* **1992**, *31*, 213.

(9) Lu, X.; Pearlstein, M. *Photochem. Photobiol.* **1993**, *57*, 86.

(10) Gülen D. *J. Phys. Chem.* **1996**, *100*, 17683.

(11) Louwe, R. J. W.; Vrieze, J.; Hoff, A. J.; Aartsma, T. J. *J. Phys. Chem. B* **1997**, *101*, 11280.

(12) Freiberg, A.; Lin, S.; Timpmann, K.; Blankenship, R. E. *J. Phys. Chem.* **1997**, *101*, 7211.

(13) Vulto, S. I. E.; Streltsov, A. M.; Aartsma, T. J. *J. Phys. Chem.* **1997**, *101*, 4845.

(14) Savhikin, S.; Buck, D. R.; Struve, W. S. *Biophys. J.* **1997**, *73*, 2090.

(15) Kühn, O.; Sundström, V. *J. Chem. Phys.* **1997**, *107*, 4154.

(16) Kühn, O.; Renger, Th.; Pullerits, T.; Voigt, J.; May, V.; Sundström, V. *Trends Photochem. Photobiol.* **1997**, *4*, 213.

(17) Xiche, Hu; Ritz, T.; Damjanovich, A.; Schulten, K. *J. Phys. Chem. B* **1997**, *101*, 3854.

(18) Spano, F. C. *Phys. Rev. Lett.* **1991**, *67*, 3424.

(19) Knoester, J.; Spano, F. C. *Phys. Rev. Lett.* **1995**, *74*, 2780.

(20) Chernyak, V.; Mukamel, S. *J. Opt. Soc. Am. B* **1996**, *13*, 1302.

(21) Chernyak, V.; Wang, N.; Mukamel, S. *Phys. Rep.* **1995**, *263*, 213.

(22) Kühn, O.; Chernyak, V.; Mukamel, S. *J. Chem. Phys.* **1996**, *105*, 8586.

(23) Kühn, O.; Mukamel, S. *J. Phys. Chem. B* **1997**, *101*, 809.

(24) Renger, Th.; May, V. *Phys. Rev. Lett.* **1997**, *78*, 3406.

(25) Renger, Th.; May, V. *Photochem. Photobiol.* **1997**, *66*, 618.

(26) Renger, Th.; May, V. *J. Phys. Chem. B* **1997**, *101*, 7211.

(27) Kühn, O.; Sundström, V. *J. Phys. Chem. B* **1997**, *101*, 3432.

(28) Lutz, M.; Hoff, A. J.; Brehamet, L. *Biochim. Biophys. Acta* **1982**, *679*, 331.

(29) May, V.; Schreiber, M. *Chem. Phys. Lett.* **1991**, *181*, 267. Kühn, O.; May, V.; Schreiber, M. *J. Chem. Phys.* **1994**, *101*, 10404.

(30) Jean, J. M.; Friesner, R. A.; Fleming, G. R. *J. Chem. Phys.* **1992**, *96*, 5827. Pollard, W. T.; Friesner, R. A. *J. Chem. Phys.* **1994**, *100*, 5054.

(31) Blum, K. *Density Matrix Theory and Applications*; Plenum Press: New York, 1981.

(32) Jean, J. M.; Fleming, G. R. *J. Chem. Phys.* **1995**, *103*, 2092.

(33) Mukamel, S. *Principles of Nonlinear Optical Spectroscopy*; Oxford: New York, 1995.

(34) Gulbinas, V.; Valkunas, L.; Kuciauskas, D.; Katilius, E.; Liuolia, V.; Zhou, W.; Blankenship, R. E. *J. Phys. Chem.* **1996**, *100*, 17950.

(35) Buck, D. R.; Savhikin S.; Struve, S. *J. Phys. Chem. B* **1997**, *101*, 8395.

(36) Pullerits, T.; Chachisvillis, M.; Sundström, V. *J. Phys. Chem.* **1996**, *100*, 10787.

(37) Scherz, A.; Parson, W. W. *Biochim. Biophys. Acta* **1984**, *766*, 666.

(38) Press, W. H.; Teukolsky, S. A.; Vetterling, W. T.; Flannery, B. P. *Numerical Recipes in Fortran*; Cambridge University Press: Cambridge, 1992.

(39) Johnson, S. G.; Small, G. J. *J. Phys. Chem.* **1991**, *95*, 471.

(40) Becker, M.; Nagarajan, V.; Parson, W. W. *Biochemistry* **1991**, *113*, 6840.

(41) Knox, R. S.; Gülen, D. *Photochem. Photobiol.* **1993**, *57*, 40.

(42) Wynne, K.; Hochstrasser, R. M. *Chem. Phys.* **1993** , *171*, 179.

(43) Chachisvilis, M. *Electronic and Vibrational Coherence in Photosynthetic and Model Systems*. PhD Thesis, Lund University, 1996. Chachisvilis, M.; Sundström, V. *J. Chem. Phys.* **1996**, *104*, 5734.

(44) This result has been recently published in Savikhin, S.; Brick, D.; Struve, W. S. *Chem. Phys.* **1997**, *223*, 303.